



Integration of functional modules in a unified photoelectrochemical device for highly efficient solar-driven cathodic metal protection

Hui Xie^a, Zhijun Wang^a, Guangyao Nie^a, Yuchen Fang^a, Weihua Li^a, Shihe Yang^{b,*},
Fa-Qian Liu^{a,*}, Zheng Xing^{a,*}

^a School of Chemical Engineering and Technology, Sun Yat-Sen University, Zhuhai 519082, China

^b Guangdong Provincial Key Lab of Nano-Micro Material Research, School of Advanced Materials, Peking University Shenzhen Graduate School, Shenzhen 518055, China

ARTICLE INFO

Keywords:

Energy conversion
Directional charge migration
Metal protection
Semiconductors
Solar-powered devices

ABSTRACT

The ever-increasing energy consumption stimulated the development of various solar energy conversion systems. Photocathodic protection (PCP), emerges as a promising photoelectrochemical technology to alleviate metal corrosion, but the centralization of all core reaction steps on one photoelectric-conversion-unit induces extremely low energy conversion efficiencies. Herein, a proof-of-concept modular PCP device incorporating electron transport layer (ETL), photoelectric conversion layer (PCL), hole transport layer (HTL) and hole consumption layer (HCL) is fabricated to delocalize the key reaction steps for the first time. Such a unified ETL/PCL/HTL/HCL architecture facilitates the efficient extraction of photoexcited electrons from the small-gap PCL to the protected metal through ETL, and holes to HCL for water oxidization through HTL. The directional “macroscopic” charge migration, prolonged charge lifetime and accelerated water oxidation lead to significantly improved PCP effectiveness in simulated seawater. Our findings provide a groundbreaking PCP design, allowing fine-tuning individual functional modules and inter-modular interfaces to vastly elevate performance.

1. Introduction

In response to the global energy crisis, various photoelectrochemical (PEC) conversion systems have been designed since the last century to efficiently utilize solar energy to drive up-hill chemical reactions, including water splitting, CO₂ reduction, N₂ fixation, transformation of organic compounds, etc. [1–7]. Photocathodic protection (PCP), an emerging PEC technology that employs semiconducting materials in the form of photoanodes or coatings to achieve solar-electric-chemical conversion and provide anti-corrosion cathodic currents to metals, has been gaining increasing attention [8], especially for the maintenance of underwater metallic facilities, such as offshore wind turbines, port buildings, ships, bridge piers, etc. Metals tend to lose electrons irreversibly in nature, a process commonly known as metal corrosion, which has caused serious worldwide economic and social losses [9]. The application of conventional cathodic metal protection methods, including impressed current cathodic protection (ICCP) and sacrificial anode cathodic protection (SACP) in the marine environment is hindered by the drawbacks such as additional electricity input from the

grid, material loss, release of pollutants, and inconvenient maintenance [10]. In this regard, PCP systems, especially the photoanode-typed PCP systems, represent a convenient, low-cost and environmentally friendly technology and open up new horizons for metal protection in the future.

Up to now, a few key factors still restrict the practical application of PCP: (1) insufficient utilization of the overall sunlight spectrum, (2) severe recombination of the photogenerated charge carriers, (3) sluggish surface reaction involving holes. Therefore, a series of works have been conducted to address those limiting factors via elemental doping [11, 12], morphological tuning [13,14], and heterostructuring [15–21]. Doping can strengthen the light-harvesting capability of semiconductors, but was often accompanied by increased charge recombination. Morphological tuning facilitates certain carrier transportation and expands semiconductor-electrolyte interface, but has negligible effect on light absorption or oxidation reaction thermodynamics. Heterojunctions are designed to establish an internal electric field (IEF) to promote electron-hole pair separation, but such charge separation is only localized near the interface between different semiconductor nanoparticles. From the perspective of a photoanode as a unity, the

* Corresponding authors.

E-mail addresses: chsyang@pku.edu.cn (S. Yang), liufq7@mail.sysu.edu.cn (F.-Q. Liu), xingzh7@mail.sysu.edu.cn (Z. Xing).

<https://doi.org/10.1016/j.apcatb.2024.124164>

Received 3 March 2024; Received in revised form 30 April 2024; Accepted 5 May 2024

Available online 8 May 2024

0926-3373/© 2024 Elsevier B.V. All rights reserved.

charge diffusion behavior at the macroscopic level is generally disordered and non-directional due to the sufficient mixing of two materials. Thus, similar to single phase photoanodes, the “correct flow direction” of charge carriers, that is, electrons to the external circuit and finally to the protected metal, and holes to the electrolyte, in heterostructured photoanodes are solely attributable to the energy band bending at the semiconductor-electrolyte interface [22], which cannot guarantee all the photoexcited electrons being driven out of the photoanode. In addition, although the slow oxidation reaction kinetics on the

semiconductor surface leads to the accumulation of holes and consequently shortened lifetime of the photogenerated electrons [23,24], it has been largely overlooked in the past. It remains a huge challenge to address the abovementioned key issues all at once via the reported strategies.

Fundamentally, since all the core reaction steps of conventional PCP systems occur on a single photoelectric conversion unit (a single or composite semiconductor), that is, from photon capture, exciton generation, electron-hole pair separation, charge diffusion, to electron flow-

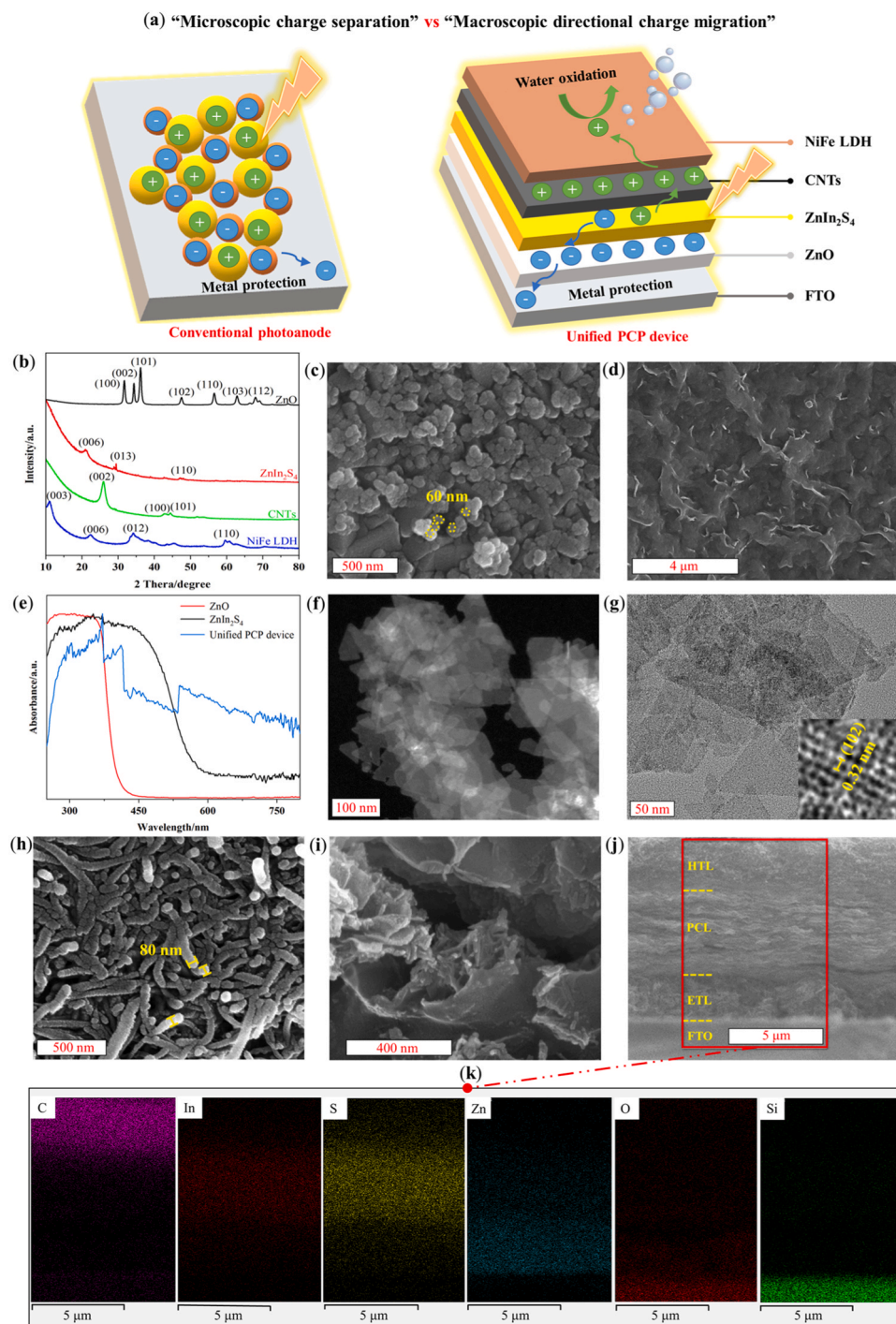


Fig. 1. (a) schematic illustration of charge separation in a conventional heterostructured photoanode as compared to that in a unified PCP device with integrated functional modules; (b) XRD patterns of ZnO NPs, ZIS NSs, CNTs and NiFe LDH NFs; SEM images of (c) ZnO NPs and (d) ZIS NSs; (e) UV-vis diffuse reflectance spectra of ZnO NPs, ZIS NSs and the unified PCP device; (f) HAADF-STEM and (g) HRTEM images of ZIS NSs; SEM images of (h) CNTs and (i) NiFe LDH NFs; (j) cross-sectional SEM image and (k) corresponding EDS elemental maps of FTO/ETL/PCL/HTL.

out and oxidization of species in the electrolyte (OH^- or H_2O) with holes, it is difficult to optimize all the reaction steps simultaneously. Inspired by the classic “n-i-p” structure of photovoltaic cells [25–28], we have designed a new type of PCP system, in which independent functional modules including electron transport layer (ETL), photoelectric conversion layer (PCL), hole transport layer (HTL) and hole consumption layer (HCL) are sequentially assembled to a unified device. In this next-generation PCP system, the nanoscale architecture allows the break-down of all PCP reaction steps: a semiconducting material (PCL) is carefully chosen to absorb photons and generate excited charge carriers, an electron conducting material (ETL) and a hole conducting material (HTL) placed on the opposite sides of the PCL quickly extract the electrons and holes from the PCL, respectively, and a hole consumption material located at the outmost layer (HCL) accepts the holes from the neighboring HTL and efficiently catalyzes the oxidation reactions that occur at the device-electrolyte interface. To demonstrate the feasibility of the modular PCP system, a proof-of-concept device was constructed in this work. As shown in Fig. 1a, ZnIn_2S_4 (ZIS) was selected as the PCL material on account of its low toxicity and unique semiconductor characteristics including broad optical absorption range, high absorption coefficient, excellent charge transfer kinetics associated with its 2D crystal structure [29], etc., n-type ZnO nanoparticles (NPs), carbon nanotubes (CNTs) and nickel-iron layered double hydroxide nanoflakes (NiFe LDH NFs) were employed as the ETL, HTL and HCL materials, respectively. Unlike conventional heterostructured photoanodes composed of mixed semiconductor NPs, the IEFs in the as-fabricated modular PCP device are built between adjacent layers instead of between particles in direct contact, and thus the charge carriers are manipulated to flow in a consistent direction throughout the whole device. In addition, the NiFe LDH NFs that were deposited on the very top of the modular device as the HCL, significantly improved the interfacial oxygen evolution reaction (OER) kinetics and minimized accumulation of excessive holes, which not only prolonged the lifetime of electrons and consequently increased the energy conversion efficiency, but also boosted the stability of the device in the absence hole scavengers. Although small-gap semiconductors such as CdS and ZIS with excellent light absorption properties suffer severe photo-degradation in electrolyte, the multi-module structure provide extra protection to ZIS, afforded by the screening effect of HTL and HCL. Therefore, in this brand-new PCP architecture, the optimization of individual modules (reaction steps) and interaction between neighboring modules brought about significant upgrades for cathodic metal protection performance compared to the traditional systems.

2. Experimental section

2.1. Preparation of ZIS NSs

According to the reference [30–32], $\text{Zn}(\text{CH}_3\text{COO})_2 \cdot 2\text{H}_2\text{O}$ (0.6 mmol) and InCl_3 (1.2 mmol) were dissolved into 100 mL deionized water and stirred for 30 min. Subsequently, excessive thioacetamide (3.2 mmol) was added into the above solution and stirred for another 30 min. The solution was then heated to 95°C and kept vigorous stirring at this temperature for 5 h. After that, the as-synthesized product was collected by centrifugation, washed with deionized water twice and further redispersed into 80 mL H_2O with 60 min continuously sonication to obtain the final dispersion.

2.2. Synthesis of NiFe LDH NFs

NiFe LDH NFs were prepared by hydrothermal method in terms of previous reports [33,34]. Briefly, 0.3 g $\text{Ni}(\text{NO}_3)_2 \cdot 6\text{H}_2\text{O}$, 0.4 g $\text{Fe}(\text{NO}_3)_3 \cdot 9\text{H}_2\text{O}$ and 0.3 g urea were mixed in 80 mL deionized water. After dissolution, the solution was poured into a 100 mL autoclave and heat at 120°C for 12 h. After allowing the autoclave to cool naturally to room temperature, the as-synthesized product was collected by

centrifugation and washed with deionized water three times, then dry naturally in the air.

2.3. Assembly of FTO/ETL/PCL/HTL/HCL

FTO (Fluorine-doped Tin Oxide) glass ($1.5\text{ cm} \times 2\text{ cm} \times 2.2\text{ mm}$, working area as 1.5 cm^2) was cleaned in an ultrasonic bath with acetone, ethanol, deionized water for 30 min, respectively. Then treated by plasma for 30 min to further clean the surface and improve spreadability of solvents. The ETL was spin-coated onto FTO at 3000 rpm for 60 s using the dispersion of $15\text{ mg} \cdot \text{mL}^{-1}$ ZnO NPs in ethanol, then vacuum dried at 80°C for 2 h. After cooling to room temperature, the PCL was dropped on top of the ETL using the ZIS NSs dispersion ($2.2\text{ g} \cdot \text{mL}^{-1}$) synthesized above and overnight in a vacuum oven at 35°C . HTL ($1.75\text{ wt}\%$ CNTs in aqueous solution) was spin-coated onto the PCL film at 3000 rpm for 30 s. After that, the film was vacuum dried at 35°C for 2 h. Finally, $10\text{ }\mu\text{L}$ NiFe LDH NFs-ethanol dispersion (the amount of HCL is $1.1\text{ wt}\%$ verses to PCL) was dropped on the HTL and vacuum dried at 35°C for 30 min to obtain the FTO/ETL/PCL/HTL/HCL.

3. Results and discussion

3.1. Fabrication of the unified PCP device incorporating functional modules

Fig. S1 displays the overall fabrication process of the unified PCP device onto a conducting FTO glass substrate. Commercial hexagonal phase (Fig. 1b, JCPDS No. 80–0074) ZnO NPs with an average diameter of approximately 60 nm (Fig. 1c) were first spin-coated on the FTO glass as the ETL. The ultrathin ZIS nanosheets (NSs) (Fig. 1d) prepared by a facile low-temperature refluxing method, which showed strong visible light absorption with an absorption edge at ca. 574 nm (Fig. 1e), as indicated by the UV–vis spectrum, were then drop-casted onto FTO/ETL as the PCL. As shown in Fig. 1f, the image recorded with high-angle annular dark-field scanning transmission electron microscopy (HAADF-STEM) verified the ultrathin nature of the ZIS NSs, and the lateral dimensions were around tens of nanometers. In the XRD pattern, three peaks at $2\theta = 21.3$, 28.9 and 47.2° corresponding to the (006), (013) and (110) planes of hexagonal phase (JCPDS No. 65–2023, P-3m1 (164) group, $a = b = 3.85\text{ }\text{\AA}$, $c = 24.68\text{ }\text{\AA}$), respectively [30,31], were observed. The distinct lattice fringes of ca. 0.32 nm observed in the high-resolution TEM (HRTEM) image (Fig. 1g inset) correspond to the (102) crystallographic plane of ZIS NSs [30]. The X-ray photoelectron spectroscopy (XPS) scan (Fig. S2) showed that ZIS NSs was mainly composed of Zn, In and S elements, which is consistent with the energy dispersive spectrometer (EDS) elemental mapping results (Fig. S3). The high-resolution spectra of Zn 2p, In 3d and S 2p further verified the successful synthesis and deposition of ZIS: the observed peaks at 1045.7 and 1022.6 eV were assigned to the Zn $2p_{1/2}$ and Zn $2p_{3/2}$ doublets, respectively; the $3d_{3/2}$ and $3d_{5/2}$ doublets of In 3d were located at 453.1 and 445.5 eV, respectively; two S 2p peaks appeared at 163.4 ($2p_{1/2}$) and 162.3 eV ($2p_{3/2}$) [30]. Commercial hexagonal phase (JCPDS No. 75–1621) CNTs with an average diameter of about 80 nm (Fig. 1h), was directly deposited onto the FTO/ETL/PCL structure via spin coating as the HTL, forming a reticular structure through intertwining of individual CNTs. Finally, the α -phase [33] NiFe LDH NFs (Fig. 1i and Fig. S4) synthesized via wet chemical protocols, was used to decorate the topmost surface of FTO/ETL/PCL/HTL as the HCL. Thereby, through such a bottom-up layer-by-layer assembly strategy, a FTO/ETL/PCL/HTL/HCL nanoarchitecture was established. As expected, the cross-sectional SEM image of FTO/ETL/PCL/HTL (Fig. 1j) revealed a multilayer structure, which were further verified by the corresponding EDS elemental maps (Fig. 1k): the layer located directly above the FTO glass substrate (containing Si and O elements) exhibited clear signals of Zn and O, indicating that this layer is composed of ZnO

NPs; besides Zn, the second layer from the bottom contained more In and S elements, suggesting its chemical nature of ZIS; C elements were uniformly distributed at the top layer, originating from the CNTs. Thus, via the sequential deposition of ZnO NPs, ZIS NSs and CNTs on the FTO substrate, the designed FTO/ETL/PCL/HTL nanoarchitecture was successfully built.

3.2. Evaluation of PEC conversion efficiency and PCP performance

Since the metal protection efficiency of PCP systems is directly related to the PEC conversion process of the photoanodes, the PEC characteristics of the as-prepared unified device comprising multiple modules have been thoroughly investigated (see Fig. S5 for the testing set-up). The open circuit voltage (OCV) of all photoelectrodes in 3.5 % NaCl solution under intermittent illumination (light on for 100 s and light off for 100 s per cycle) was monitored. As displayed in Fig. 2a-c, the steady OCV values of ETL and all types of electrodes containing PCL shifted negatively (from 0.50 to 0.29 V vs. *RHE* for FTO/ETL, from 0.47 to 0.06 V vs. *RHE* for FTO/PCL, from 0.47 to -0.03 V vs. *RHE* for FTO/

ETL/PCL, from 0.49 to -0.10 V vs. *RHE* for FTO/ETL/PCL/HTL, from 0.48 to -0.23 V vs. *RHE* for FTO/ETL/PCL/HTL/HCL in the 1th cycle) when external irradiation was introduced, due to the accumulation of photoexcited electrons, typical for n-type semiconductors (both ZnO NPs and ZIS are n-type semiconductors). Compared to the photoinactive HTL and FTO/ETL that only produced an small open-circuit photovoltage (OCP, the rapid change of OCV upon irradiation) of -0.21 V (1th cycle), the much larger OCP of FTO/PCL (-0.41 V, 1th cycle) was further increased with the stepwise incorporation of more functional modules (-0.50 V for FTO/ETL/PCL, -0.59 V for FTO/ETL/PCL/HTL and -0.71 V for FTO/ETL/PCL/HTL/HCL, 1th cycle), which hints an improved separation of photoexcited charge carriers. It is noteworthy that upon irradiation, the charge transport material-assisted PCL structure noticeably shortened the time for the OCV to stabilize, revealing the capabilities of ETL and HTL to rapidly extract and transfer photogenerated carriers from PCL. The photocurrents measured via linear sweep voltammetry (LSV) under intermittent illumination are depicted in Fig. 2d. Negligible current was detected for the bare FTO substrate in the potential range from -0.35–1.30 V vs. *RHE* due to the

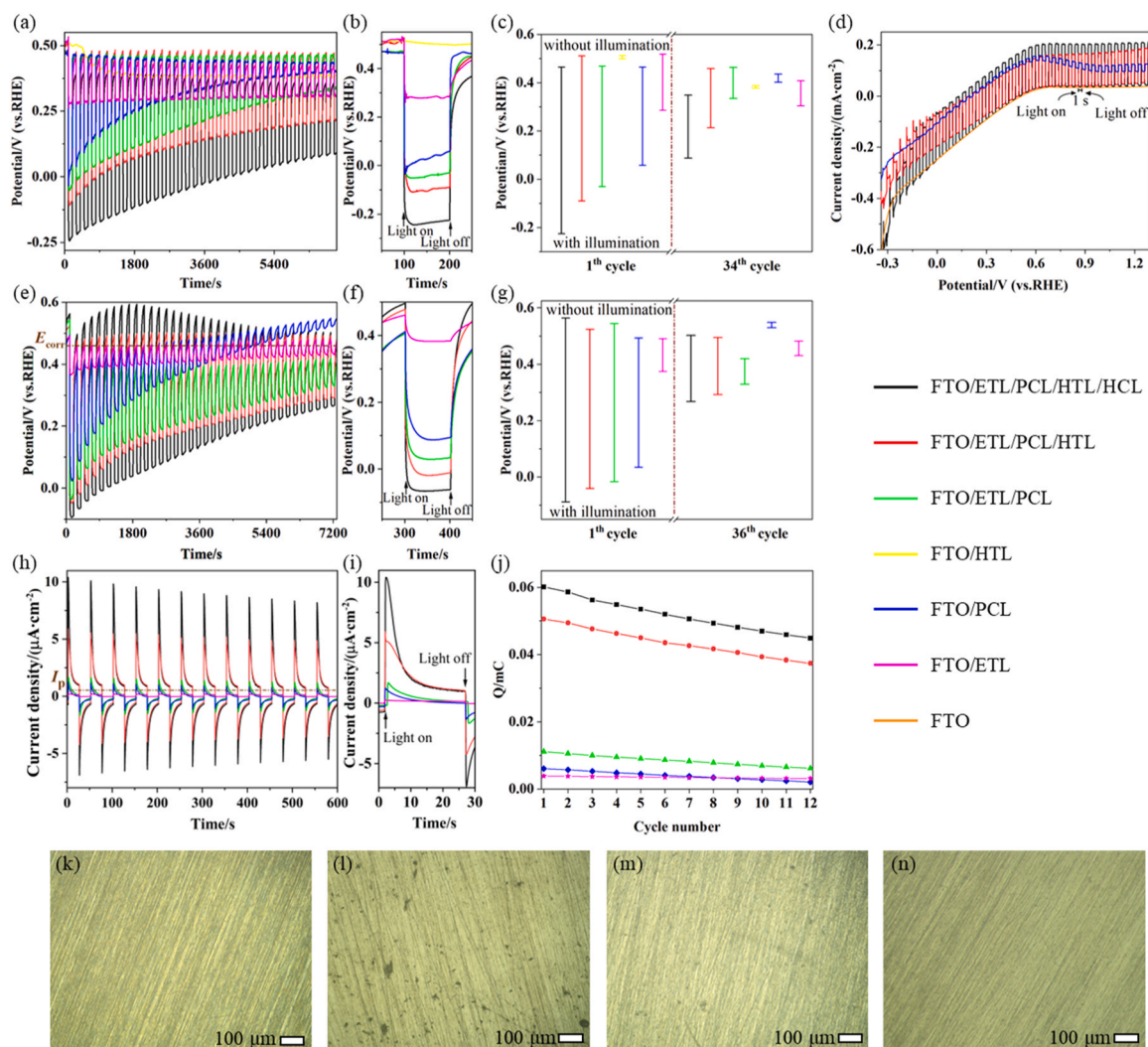


Fig. 2. (a) OCV monitored continuously, (b) the corresponding enlarged plots of the 1th light on/off cycle, (c) the corresponding OCV values with and without illumination during the 1th & 34th light on/off cycle and (d) LSV plots of various photoanodes tested under intermittent illumination; (e) OCV monitored continuously, (f) the corresponding enlarged plots of the 2th light on/off cycle and (g) the corresponding OCV values with and without illumination during the 1th & 36th light on/off cycle of 304 SS electrically connected with various photoanodes under intermittent illumination; (h) time profiles of current density and (i) the corresponding enlarged plots of the 1th light on/off cycle measured between various photoanodes and 304 SS, and (j) the corresponding Q injected into 304 SS from various photoanodes during each light on/off cycle with a two-electrode set-up under intermittent illumination; Metalloscope photos of (k) pristine, (l) 304 SS alone immersed in simulated seawater, and 304 SS coupled with (m) FTO/PCL and (n) FTO/ETL/PCL/HTL/HCL after 3 h of light on/off cyclic OCV test. 3.5 % NaCl was used as the electrolyte (pH=7.0) and a 300 W xenon lamp as the light source during the measurements.

poor absorbance (Fig. S6). Unlike FTO, FTO/PCL is capable of producing low photocurrents ($0.02 \text{ mA}\cdot\text{cm}^{-2}$ at 0 V vs. *RHE*). With the establishment of a multilayer structure, FTO/ETL/PCL/HTL can generate significantly boosted photocurrent density of $0.14 \text{ mA}\cdot\text{cm}^{-2}$ at 0 V vs. *RHE*. The introduction of HCL to the outmost structure of FTO/ETL/PCL/HTL further raised the activity to another level and the photocurrent collected on FTO/ETL/PCL/HTL/HCL at 0 V vs. *RHE* reached $0.20 \text{ mA}\cdot\text{cm}^{-2}$. Such remarkably boosted photocurrent produced by the multi-modular structure not only reflected the increased energy conversion efficiency, but more importantly, implied the fact that the photogenerated charges within PCL migrated in the “correct direction” throughout the unified device as designed and outflowed eventually. The benefit of this stacked-module architecture for the photostability of ZIS NSs has also been illustrated via monitoring the OCV values over extended illumination (Fig. S7). While the OCV of FTO/PCL under continuous irradiation gradually shifted from 0 to 0.50 V (vs. *RHE*) in 2 hours due to the oxidation of sulfides in direct contact with the electrolyte [35], FTO/ETL/PCL/HTL showed milder OCV retracement (from -0.12 – -0.31 V vs. *RHE*). The OCV of FTO/PCL and FTO/ETL/PCL/HTL monitored under intermittent illumination (Fig. 2a) and the corresponding OCP decay profile over 35 light on/off cycles (Fig. S8) further verified the fact that the stacked-module architecture can provide a more stable microenvironment for the photoabsorbing semiconductors.

The drastically improved solar-electric-chemical conversion capabilities as demonstrated by the unified architecture and its accommodated long-term stability for sulfides greatly encouraged us to investigate the PCP performance of the FTO/ETL/PCL/HTL/HCL modular system. 304 stainless steel (304 SS), one of the most versatile and widely used metallic material, was chosen as the target metal to evaluate the PCP performance of the as-prepared samples. In principle, a PCP system should initiate metal protection if it can pull the electrochemical potential of a metal below its self-corrosion potential (E_{corr}), in the case of 304 SS, 0.46 V vs. *RHE* as obtained from the Tafel curve (Fig. S9). However, based on research on the conventional ICCP technology, only when a photoanode can drive the metal potential to shift negatively 200–300 mV than its E_{corr} , it is considered to provide sufficient protection to the metal [36,37]. Therefore, the OCV values of 304 SS (1.0 cm^2) that is electrically coupled to different PCP photoanodes (see Fig. S10 for the testing set-up) were recorded under intermittent illumination (light on for 100 s and light off for 100 s per cycle). Fig. S11 indicated that the contribution of the bare FTO substrate to PCP performance is negligible. As shown in Fig. 2e–g, while ZnO is a semiconducting material, FTO/ETL merely caused tiny OCV change to 304 SS (from 0.46 to 0.38 V vs. *RHE* in the 2th cycle, from 0.48 to 0.43 V vs. *RHE* in the 36th cycle) upon illumination, which may originate from the limited light-harvesting capacity. FTO/PCL can initially produce an OCP of -0.32 V and shift the OCV of 304 SS to 0.03 V vs. *RHE* (2th cycle), but the OCP gradually dropped to -0.03 V and the OCV was pulled to 0.52 V vs. *RHE* after 36 cycles, which cannot guarantee proper PCP. Adding ETL below PCL not only enlarged the OCP to -0.38 V (2th cycle), but also led to a more negative photoinduced OCV of 0.03 V vs. *RHE* (2th cycle) to the 304 SS connected to FTO/ETL/PCL. However, similar to FTO/PCL, the photocorrosion of sulfides in FTO/ETL/PCL due to the exposure of PCL to the electrolyte led to quick positive shift of the OCV signals of 304 SS connected to FTO/ETL/PCL under irradiation (0.33 V vs. *RHE* in the 36th cycle with a reduced OCP of -0.09 V). In addition, although CNTs itself is not photoactive, upon the introduction of HTL, the PCP performance of FTO/ETL/PCL/HTL was steadily enhanced, with a OCP of -0.48 V and a stable OCV of -0.01 V vs. *RHE* (2th cycle) under irradiation. Moreover, it can be seen that the OCV upshifting of 304 SS under illumination originated from the photocorrosion of sulfides is largely mitigated (OCP of -0.20 V and OCV of 0.29 V vs. *RHE* in the 36th cycle), which is likely due to the shielding effect of HTL. The deposition of HCL further elevated the level of solar-powered cathodic protection. Impressively, FTO/ETL/PCL/HTL/HCL can not only generate an OCP as large as -0.56 V when coupled with 304 SS and

bring the OCV of 304 SS down to as low as -0.07 V vs. *RHE* in the 2th cycle, but also maintain the OCV of metal more than 200 mV below its E_{corr} (0.26 V vs. *RHE*) even in the 36th cycle. Thus, the gradual integration of more functional modules induced increasing thermodynamic power for the protection of 304 SS.

Conventional cathodic protection systems inject a current (protection current, I_p) to the metal (cathode) to make the metal “immune” to corrosion. It has been pointed out in previous studies that cathodic protection can be realized with the I_p of 0.1 – $0.2 \text{ }\mu\text{A}\cdot\text{cm}^{-2}$, and the recommended value is $0.5 \text{ }\mu\text{A}\cdot\text{cm}^{-2}$ [38,39]. In order to probe the actual photocurrents that different PCP architectures can produce and inject to 304 SS for cathodic protection, the current vs. time curves were collected with a two-electrode set-up (see Fig. S12 for the testing set-up) at 0 V bias under intermittent illumination (12 light on/off cycles, light on for 25 s and light off for 25 s per cycle). Fig. S13 demonstrated that the FTO substrate can only supply several nA of photocurrent. As shown in Fig. 2h,i, FTO/PCL produced an instantaneous photocurrent density of $1.25 \text{ }\mu\text{A}\cdot\text{cm}^{-2}$ upon irradiation, which rapidly dropped and stabilized at $0.20 \text{ }\mu\text{A}\cdot\text{cm}^{-2}$ in the 1th cycle. The photocorrosion of PCL led to quick decline of photocurrent and no detectable current was generated after 12 test cycles (Fig. S14). Low levels of photocurrents were also detected with FTO/ETL (stabilized photocurrent density of $0.17 \text{ }\mu\text{A}\cdot\text{cm}^{-2}$ in the 1th cycle, and $0.13 \text{ }\mu\text{A}\cdot\text{cm}^{-2}$ in the 12th cycle). Adding ETL to FTO/PCL did not induce significant improvement in photocurrent (the instantaneous photocurrent density of $1.67 \text{ }\mu\text{A}\cdot\text{cm}^{-2}$ upon irradiation was gradually stabilized at $0.43 \text{ }\mu\text{A}\cdot\text{cm}^{-2}$ in the 1th cycle) or suppress photocurrent decay during the testing process (stabilized photocurrent density of $0.18 \text{ }\mu\text{A}\cdot\text{cm}^{-2}$ in the 12th cycle). However, both FTO/ETL/PCL/HTL and FTO/ETL/PCL/HTL/HCL exhibited enhanced PCP performance in terms of both energy conversion efficiency and photostability, with noticeably larger photocurrents (the instantaneous photocurrent densities reached 5.91 and $10.37 \text{ }\mu\text{A}\cdot\text{cm}^{-2}$ respectively, and then both stabilized at $1.73 \text{ }\mu\text{A}\cdot\text{cm}^{-2}$ in 1th cycle, and at $1.17 \text{ }\mu\text{A}\cdot\text{cm}^{-2}$ in 12th cycle for both), to maintain the sufficient cathodic protection of 304 SS ($I_p > 0.5 \text{ }\mu\text{A}\cdot\text{cm}^{-2}$). Moreover, since the quantities of electric charge (Q) is a function of “current density” and “time”, namely, $Q = it$, via integrating the photocurrent densities produced during the 25 s illumination, the actual Q injected into 304 SS from various photoanodes during the cyclic test can be calculated. As shown in Fig. 2j, FTO/ETL/PCL/HTL/HCL kept supplying drastically larger Q to 304 SS (0.060 and 0.045 mC in the 1th and 12th cycle, respectively) than the other photoanodes (0.050, 0.011, 0.006 and 0.004 mC for FTO/ETL/PCL/HTL, FTO/ETL/PCL, FTO/PCL and FTO/ETL, respectively in the 1th cycle; 0.037, 0.006, 0.002 and 0.003 mC for FTO/ETL/PCL/HTL, FTO/ETL/PCL, FTO/PCL and FTO/ETL, respectively, in the 12th cycle), and the photoanodes with more complete configuration of functional modules were capable of outputting greater electric power to protect 304 SS. These results are also consistent with the Tafel curves of the 304 SS coupled to various photoanodes under illumination (Fig. S9). With the increased function layers of the coupling photoanodes, the mixed potentials of 304 SS gradually shifted negatively (0.03, 0.16, 0.37, 0.45 V vs. *RHE* for FTO/ETL/PCL/HTL/HCL, FTO/ETL/PCL/HTL, FTO/ETL/PCL and FTO/PCL, respectively) and the mixed photocurrent became enlarged. To directly visualize the overall PCP effectiveness of the unified device, the corrosion evolution of 304 SS under different conditions were presented with metaloscope photos. When fresh 304 SS was immersed alone in simulated seawater, its corrosion-free smooth surface (Fig. 2k) experienced severe pitting corrosion (Fig. 2l) after 3 h of light on/off cyclic OCV test. Under the protection of FTO/PCL, FTO/ETL/PCL or FTO/ETL/PCL/HTL, the pitting corrosion of 304 SS (Figs. 2m & S15) was alleviated, and the 304 SS even maintained its pristine state if electrically coupled with FTO/ETL/PCL/HTL/HCL (Fig. 2n), which is in good agreement with the electrochemical evaluation results.

Table S1 summarized the comparison of PCP performance between the as-prepared unified device and representative photoanodes that

have been previously reported. However, it should be noted that it is almost impossible to make scientific comparisons currently for four reasons: (1) the sizes of the photoanodes and protected metals varied in different works, and relationship between the sizes and the PCP performance is not necessarily linear; (2) almost all the previous works measured the mixed photocurrent of the metal coupled to the photoanode, rather than the actual injected photocurrent from the photoanode to the metal; (3) the addition of sacrificial agents such as Na_2S to the electrolyte can noticeably enhance the measured PCP performance, but it does not reflect the real capability of a system; and (4) various light sources were used in different works. Furthermore, to demonstrate the applicability of this unified device, the PCP performance for other commonly used metals including 316 SS, 403 SS and Q235 carbon steel (CS) were evaluated. As shown in Fig. S16 and S17, the multilayer architecture provided similar PCP performance to 316 SS and 403 SS as to 304 SS. With the light was turned on, the OCVs of 316 SS and 403 SS decreased to 0.07 and -0.03 V vs. *RHE*, respectively, and the photocurrent densities of 5.33 and $11.52 \mu\text{A}\cdot\text{cm}^{-2}$ can be injected into 316 SS and 403 SS, respectively, which are enough to initiate cathodic protection. The unified PCP system can only lower the potential of Q235 CS by 150 mV under illumination, which can be attributed to the inherently negative E_{corr} of carbon steel, making it thermodynamically difficult to inject electrons. The long-term operational stability of the unified PCP device was also evaluated in natural seawater under intermittent illumination (light on for 100 min and light off for 100 min per cycle). As shown in Fig. S18, the as-prepared device can pull the OCV of 304 SS from 0.59 V (vs. *RHE*) down to 0.06 V (vs. *RHE*) upon irradiation in the 1th cycle with an OCP of -0.53 V. After the 1th cycle, the OCP of each cycle gradually decreased and stabilized at about -0.1 V after the 7th cycle. The decay of the PCP efficacy may be attributed to the penetration of seawater. Additionally, this unified PCP device was post-characterized by XRD, XPS, SEM and EDS techniques. The XPS results

(Fig. S19) show that the photoanode outer surface before and after the PCP performance evaluation is mainly composed of C elements (from the HTL), and tiny Ni elements from the HCL were also detected, while the XRD patterns (Fig. S20) suggest that the detachment of HCL from the photoanode may occur after testing. The SEM images (Fig. S21&S22) suggest the stability of the sandwich structure, but the EDS signal of Cl was detected on the HTL after the PCP test, which can be attributed to the lack of device sealing.

3.3. Directional charge migration in the unified PCP device

The giant enhancement of PCP efficiency by the integration of functional modules attracted us to study the very core factor that determined the performance of any solar energy conversion systems, that is, the behaviors of photoinduced charge carriers. As shown in Fig. 3a, with the addition of ETL and HTL, the broad emission peak at 510 nm in the steady-state photoluminescence (PL) spectra of ZIS NSs is noticeably quenched, suggesting the suppression of radiative charge recombination. According to the time-resolved PL spectra (excitation wavelength: 405 nm), pure PCL exhibited rapid PL decay in nanoseconds with an average lifetime (τ_{Ave}) of 1.90 ns (Fig. 3b). With the sequential introduction of ETL and HTL, the τ_{Ave} was reduced to 1.74 and 1.40 ns, respectively, which can reveal that the charge transfer layers suppressed the annihilation of the dissociated electron-hole pairs and facilitated the spatial charge separation. Thus, smooth charge transfer channels from PCL to ETL and HTL for electrons and holes, respectively, may be established in the modular architecture, as indicated by the steady-state and transient PL results. Fig. 3c shows the plots of the derivative of OCV with respect to time versus time ($-d(\text{OCV})/dt$ vs. *t*) at the initial stage of illumination for 304 SS coupled with different photoanodes. Incorporation of more functional modules to FTO/PCL was found to gradually enlarge the $-d(\text{OCV})/dt$ value, with FTO/ETL/

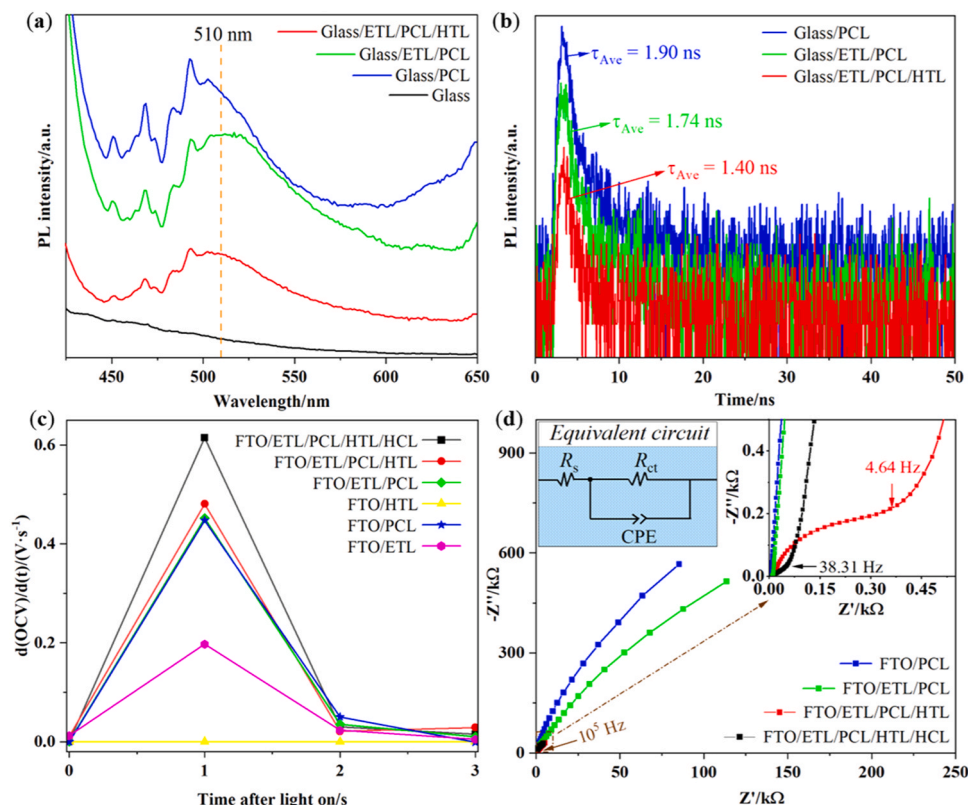


Fig. 3. (a) steady-state and (b) time-resolved PL spectra of different architectures assembled on quartz glass with the excitation wavelength of 405 nm, (c) $-d(\text{OCV})/dt$ vs. *t* plots of various photoanodes at the initial stage of illumination, (d) Nyquist plots of different photoanodes (inset shows the enlarged plot and equivalent circuit model) measured in 3.5% NaCl ($\text{pH}=7.0$).

PCL/HTL/HCL exhibiting more pronounced $-d(\text{OCV})/dt$ than other photoanodes in the first second, which suggests more efficient charge separation with the modular design, in good agreement with the PL results. In addition, electrochemical impedance spectroscopy (EIS) was employed to gain insights into the charge transfer kinetics at the photoanode-electrolyte interface. In the Nyquist plots (Fig. 3d), the charge transfer resistance at the electrode/electrolyte interface (R_{ct}), which is directly related to the interfacial electrochemical reaction rate, were extracted based on the fitted equivalent circuit model. While the Nyquist plots of FTO/PCL and FTO/ETL/PCL clearly indicated diffusion-controlled processes with almost no R_{ct} (frequency range of 10^{-2} – 10^5 Hz), FTO/ETL/PCL/HTL exhibited a R_{ct} of 570.5 Ω with a small semi-circle in the enlarged Nyquist plot (frequency range of 4.64– 10^5 Hz, inset of Fig. 3d), and a noticeably reduced R_{ct} (42.7 Ω) was observed with FTO/ETL/PCL/HTL/HCL (frequency range of 38.31– 10^5 Hz). The change of electrochemical processes on the electrode surface after the introduction of HTL and HCL onto PCL, implied faster interfacial electron transfer.

After verifying the greatly enhanced charge separation of the unified PCP device, selective photodeposition was carried out to unveil the actual transportation direction and destination of different photo-generated charge carriers within the device. The reductive photodeposition of Pt and the oxidative photodeposition of MnO_x (see SI for details) using H_2PtCl_6 and $\text{Mn}(\text{NO}_3)_2$ as the precursors, respectively, in combination with EDS elemental mapping, were designed to probe the location of electrons and holes, respectively. To rule out the influence of

ZnO NPs on the photodeposition process, visible light irradiation was used (a 300 W xenon lamp equipped with a 420 nm cut-off filter). Moreover, considering that all modules in a unified PCP device were made to cover the identical area on the FTO glass substrate, in order to avoid potential confusion caused the spatial overlapping of EDS signals from different modules, two types of architecture including FTO/ETL/PCL/HTL (classic “n-i-p” model of photovoltaic cells) and FTO/HTL/PCL/ETL (“p-i-n” model) with the bottom module (ETL or HTL, respectively) covering a larger area were deliberately fabricated for the photodeposition of MnO_x and Pt, respectively. As shown in Fig. 4a–d, after the Pt photodeposition of FTO/HTL/PCL/ETL, the EDS signals of Pt can only be found on ETL, evidencing that the photogenerated electrons in PCL can only diffuse to the ETL. Similarly, after the MnO_x photodeposition of FTO/ETL/PCL/HTL, Mn elements were solely detected on HTL (Fig. 4e–h), proving that the excited holes in PCL were selectively transferred to HTL. In order to obtain convincing evidence on the carriers’ flow direction, atomic force microscopy (AFM) and in-situ Kelvin-probe force microscopy (KPFM) analysis were performed on a specially made FTO/ETL/PCL/HTL photoanode with exposed regions of ETL, PCL and HTL. In principle, KPFM measures the contact potential difference (CPD) between the tip and the sample surface, and thus the change in CPD signals can reflect the charge accumulation or depletion in certain regions. Positive and negative CPD shifts correspond to the local accumulation of holes and electrons, respectively [40–42]. As shown in Fig. 5, under the irradiation of 445 nm, large positive CPD shifts were observed on both PCL and HTL (from 62 ± 0.05 – 701 ± 0.06 mV and from

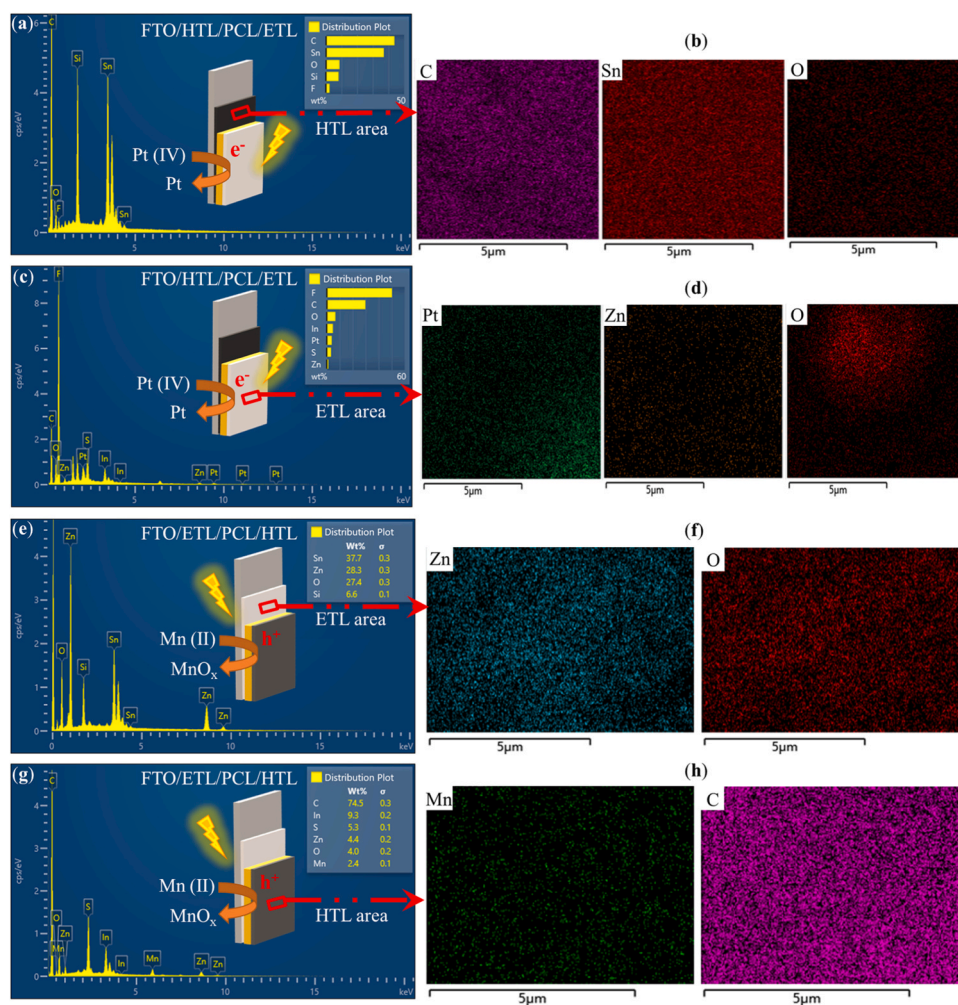


Fig. 4. (a, c) EDS element content analysis and (b, d) element mapping spectra of FTO/HTL/PCL/ETL for Pt NPs photodeposition; (e, g) element content analysis and (f, h) element mapping spectra of FTO/ETL/PCL/HTL for MnO_x NPs photodeposition.

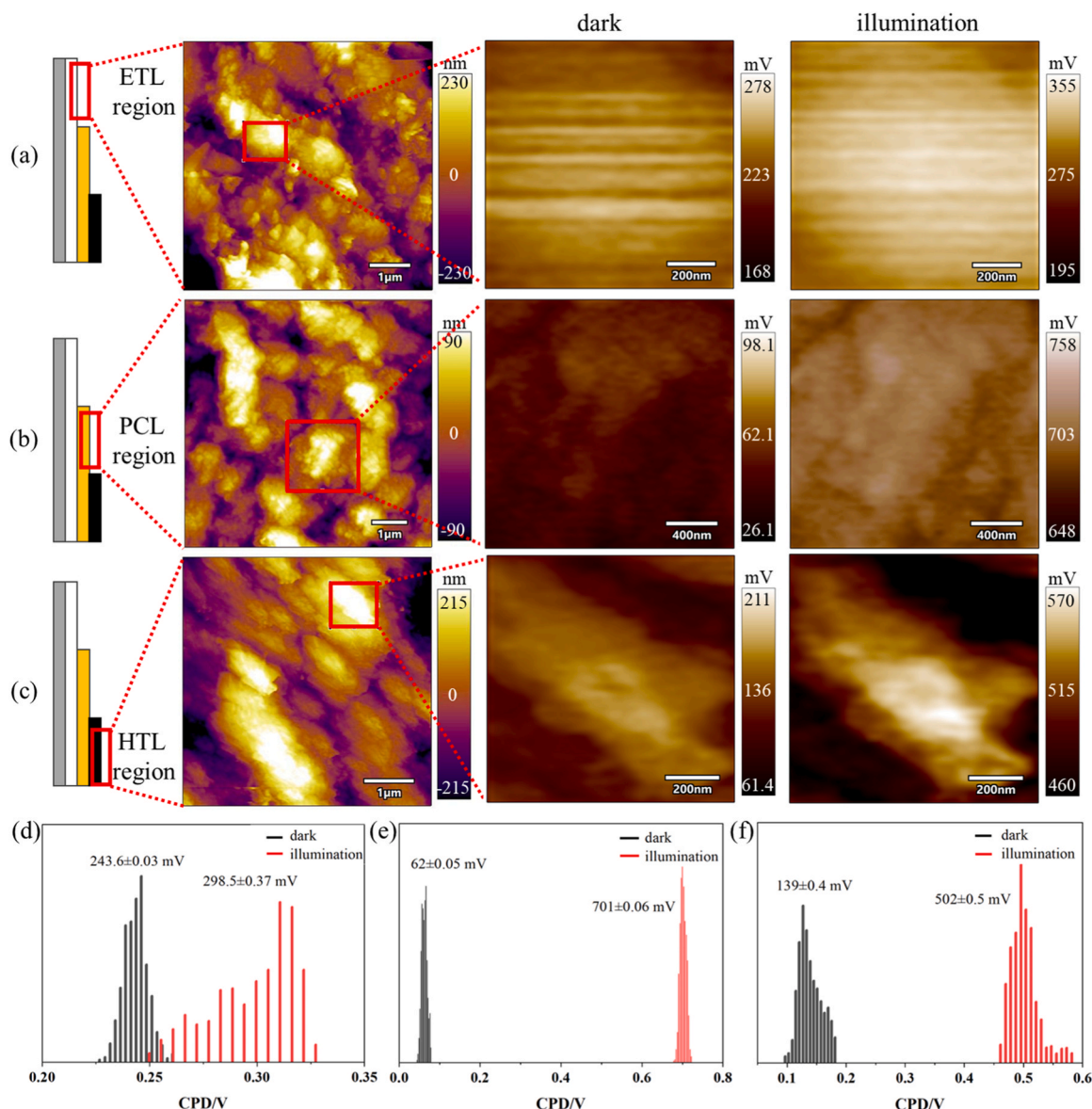


Fig. 5. AFM and in-situ KPFM images of the exposed (a) ETL, (b) PCL and (c) HTL regions of the same photoanode and the corresponding CPD distributions (marked in red boxes in the AFM images) of the exposed (d) ETL, (e) PCL and (f) HTL regions.

139 ± 0.4–502 ± 0.5 mV, respectively), but ETL only exhibited a slight positive CPD change (from 243.6 ± 0.03–298.5 ± 0.37 mV). The large positive CPD shift of HTL reflects that HTL can effectively extract holes from the neighboring PCL, while the significantly greater CPD upshift of PCL than that of ETL indicates that the electrons generated by PCL can rapidly flow into ETL and then to the FTO substrate. Therefore, through the rational design of modular architecture for the purpose of appropriate charge steering, the unified PCP device allowed for the flow of photoexcited electrons and holes in selective directions between PCL and its neighboring modules, that is, electrons to ETL and holes to HTL.

3.4. Working mechanism of the unified PCP device

The unique “navigation” of photogenerated charge carriers in the unified PCP device prompted us to further analyze the alignment of energy levels between different modules. The working function (ϕ) of PCL was estimated via measuring its secondary electron cut-off edge (SEC) using XPS spectroscopy. As shown in Fig. 6a, the ϕ of PCL was determined to be 5.12 eV relative to vacuum level, comparing with the energetics of commercial CNTs (4.90 eV relative to vacuum level) [43,

44], increasingly lower ϕ can be found from PCL to HTL, revealed a potential flow direction of photogenerated holes (from PCL to HTL). The band gaps of ETL and PCL were calculated to be 3.20 and 2.29 eV, respectively, from the Tauc plots (Fig. 6b,c). As shown in Fig. 6d, the positive slopes of Mott-Schottky (M-S) curves verified the n-type semiconducting of both ZnO NPs and ZIS NSs. The flat band potential (E_{FB}) of PCL is approximately -0.51 V vs. RHE, which is more negative than that of ETL (-0.26 V vs. RHE), suggesting that the electron transfer from PCL to ETL was thermodynamically favorable. Hence, the inter-module energy level steps can promote the transfer of photoexcited electrons from PCL to ETL and holes to HTL with IEFs, enabling selective charge extraction at both sides of PCL.

To address the suppressed hole consumption in the absence of hole scavengers, in the as-fabricated unified PCP device, an HCL is placed on the top to accelerate the surface oxidation reaction. Fig. 6e demonstrates the anodic polarization curves of FTO/ETL/PCL, FTO/ETL/PCL/HTL and FTO/ETL/PCL/HTL/HCL in 3.5 % NaCl solution (pH=7.0). In the potential range of 1.2 V to 1.8 V (vs. RHE), FTO/ETL/PCL produced rather low levels of current, which revealed the extremely sluggish oxidation reaction at the surface of ZIS NSs. While depositing HTL onto

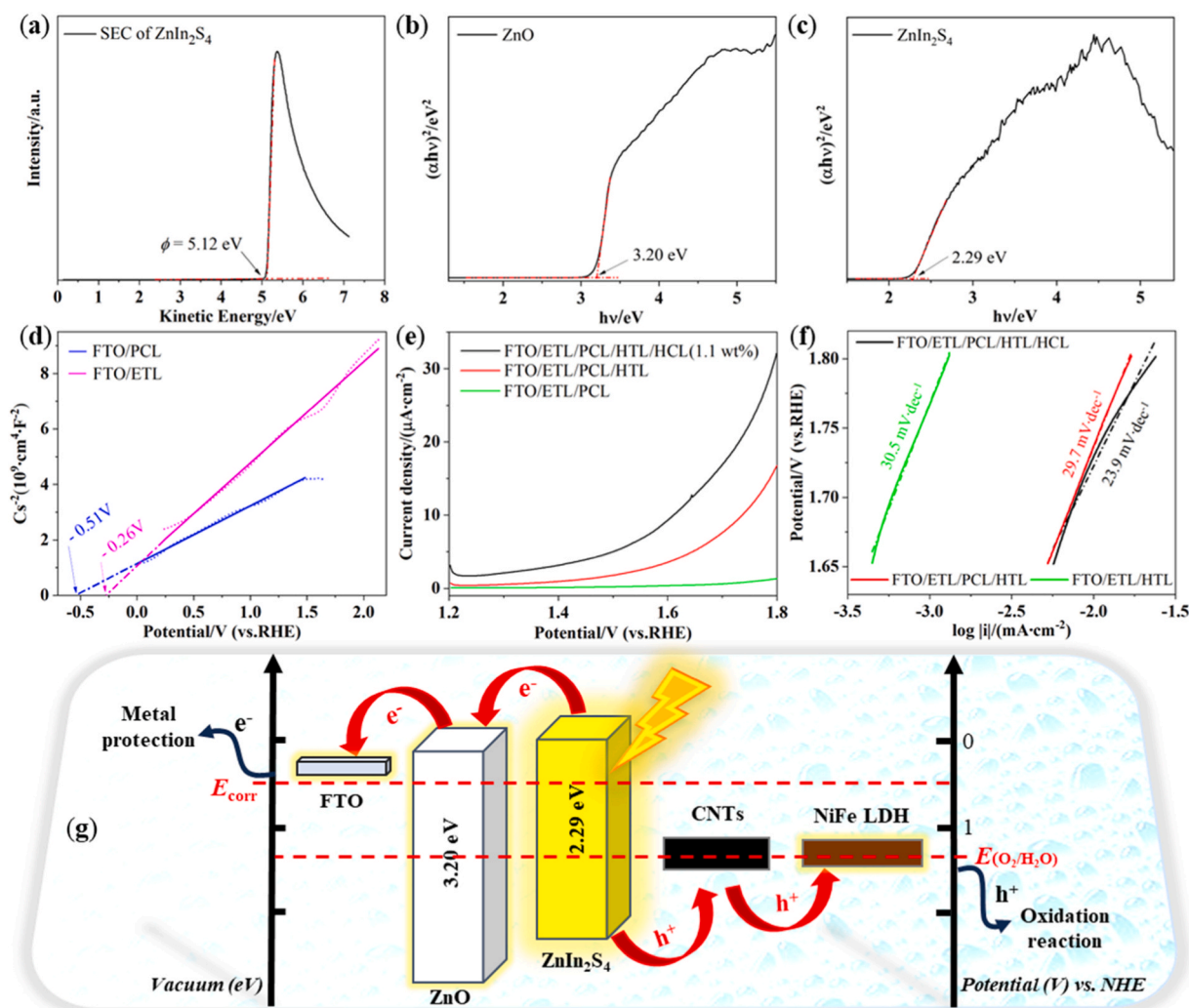


Fig. 6. (a) XPS-SEC edge spectrum of ZIS NSs; Tauc plots of (b) ZnO NPs and (c) ZIS NSs; (d) M-S curves, (e) polarization curves and (f) Tafel slopes of various photoanodes in 3.5 % NaCl (pH=7.0); (g) schematic diagram of the energy band alignment between multiple functional modules in the unified PCP device.

FTO/ETL/PCL noticeably increased the current densities, the integration of HCL further boosted the performance to even higher levels. At the current density of $5 \mu\text{A}\cdot\text{cm}^{-2}$, FTO/ETL/PCL/HTL/HCL exhibited a much lower overpotential (0.26 V) for OER as compared to FTO/ETL/PCL/HTL (0.41 V), indicating reduced thermodynamic barrier for the oxidation reaction. Additionally, FTO/ETL/PCL/HTL/HCL was analyzed to possess a smaller Tafel slope ($23.9 \text{ mV}\cdot\text{dec}^{-1}$, Fig. 6f) than FTO/ETL/PCL ($30.5 \text{ mV}\cdot\text{dec}^{-1}$) and FTO/ETL/PCL/HTL ($29.7 \text{ mV}\cdot\text{dec}^{-1}$), suggesting the faster oxidation reaction kinetics of HCL. Since no detectable Cl_2/ClO^- existed in the simulated seawater immediately after the PCP performance test (Fig. S23), it is suggested that the dominant oxidation reaction at the HCL/electrolyte interface is OER rather than chlorine evolution reaction, possibly due to the fact that the Cl^- is thermodynamically more difficult to oxidize than $\text{H}_2\text{O}/\text{OH}^-$. The drastically promoted oxidation reaction on the top surface of FTO/ETL/PCL/HTL/HCL is believed to reduce hole accumulation and consequently alleviate the recombination of dissociated electron-hole pairs.

In order to gain insights into the influence of the intrinsic electrochemical activity of electrodes on the PCP performance, the electrochemically active surface area of different photoanodes were evaluated by analyzing the double-layer capacitances [45]. The cyclic voltammetry curves (Fig. S24) of various photoanodes in simulated seawater were measured at the scan rates of 0.005, 0.01, 0.02, 0.03, 0.04 and

$0.05 \text{ V}\cdot\text{s}^{-1}$, and the capacitive currents under the same bias of FTO/ETL, FTO/ETL/PCL, FTO/ETL/PCL/HTL, FTO/ETL/PCL/HTL/HCL were recorded and plotted vs. scan rate. The specific capacitances of photoanodes obtained from the slopes (Fig. S25) are 0.009, 0.009, 0.018, and $0.0278 \text{ mF}\cdot\text{cm}^{-2}$, respectively. Since the photocurrent (Fig. 2i) supplied from FTO/ETL/PCL/HTL/HCL to 304 SS is 1.8 folds of that from FTO/ETL/PCL/HTL, 6.2 folds of that from FTO/ETL/PCL, and 61 folds of that from FTO/ETL, and the specific capacitance of FTO/ETL/PCL/HTL/HCL is 1.5 folds of that of FTO/ETL/PCL/HTL, 3.1 folds of those of both FTO/ETL/PCL and FTO/ETL, while the addition of HCL mainly introduced more electroactive sites, the establishment of the directional charge transfer architecture played a major role in the drastic PCP performance upgrade.

Based on the abovementioned analysis, the working mechanism of the unified FTO/ETL/PCL/HTL/HCL PCP architecture is illustrated in Fig. 6g. Upon irradiation, PCL generated excited electrons and holes, which were guided to selectively travel to the corresponding destinations (metal and HCL for the electrons and holes, respectively) owing to the rational alignment of energy bands. On one hand, the diffusion path of the photogenerated electrons is from PCL to ETL, then to FTO, and finally to the 304 SS (where the electrochemical potential for the metal was shifted to the corrosion-free range). On the other hand, the photogenerated holes migrated from PCL to HTL, and subsequently to HCL, where they ultimately participate in the oxidation reaction at the HCL/

electrolyte interface. Therefore, this consciously designed PCP device can overcome the fundamental bottlenecks of conventional PCP photoanodes, where partial recombination of dissociated electrons and holes inevitably occurs due to the macroscopically disordered and non-directional migration of charges.

4. Conclusions

In summary, we have developed a proof-of-concept PCP device with customized ETL/PCL/HTL/HCL modular architecture, in which various appropriate functional modules were integrated to break down all the key reaction steps of the solar-electric-chemical conversion process. The sandwiching of PCL composed of small-gap ZIS NSs by ETL and HTL composed of ZnO NPs and CNTs, respectively, not only facilitated the rapid extraction of photogenerated electrons and holes from PCL and their transportation in the opposite directions at the “macroscopic” level, but also drastically improved the stability of sulfides in PCL. In addition, the NiFe LDH NFs deposited at the outmost surface as HCL noticeably reduced the thermodynamic barrier of the oxidation reaction at the electrode-electrolyte interface, mitigating the accumulation of holes and recombination of holes with electrons. Such a rationally designed multilayer architecture and the proper alignment of energy levels between various modules ensured the directional charge flow throughout the whole PCP device, leading to a giant leap in the photoelectrochemical conversion efficiency, directly. The unified PCP device can still provide sufficient protection to 304 SS for extended test cycles, maintaining the potential of 304 SS more negative than its E_{corr} by 200 mV, and injecting a photocurrent twice of the I_p into 304 SS in simulated seawater, whereas the single PCL unit was unable to lower the potential of 304 SS below E_{corr} or inject photocurrent into the 304 SS. The universality of this unified device was also verified by evaluating the PCP performance for other commonly used metals including 316 SS and 403 SS. More importantly, the modular design employed in this work may open up new possibilities for the development of next-generation solar-driven photocathodic metal protection systems if one can optimize the material selection and fabrication protocols, or introduce new functionalities via incorporation of corresponding modules in the future. For instance, Cl^- oxidation modules may be introduced as the outmost module, which will allow researchers to not only provide PCP to metals, but also to inactivate microorganisms with the oxidized chlorine species and further alleviate metal corrosion with the reduced Cl^- concentration in seawater.

CRediT authorship contribution statement

Shihe Yang: Writing – review & editing. **Fa-Qian Liu:** Resources, Funding acquisition. **Zheng Xing:** Writing – review & editing, Supervision, Resources, Project administration, Funding acquisition. **Zhijun Wang:** Methodology. **Guangyao Nie:** Investigation. **Yuchen Fang:** Methodology. **Weihua Li:** Resources. **Hui Xie:** Writing – original draft, Methodology, Investigation, Data curation, Conceptualization.

Declaration of Competing Interest

The authors declare that they have no known competing financial interests or personal relationships that could have appeared to influence the work reported in this paper.

Data availability

Data will be made available on request.

Acknowledgements

This work was financially supported by the Natural Science Foundation of China (22202237 and 52073311), Guangdong Basic and

Applied Basic Research Foundation (2021A1515111234 and 2023A1515011552), and Guangdong-Hong Kong-Macao Joint Innovation Field Research Foundation (2023A0505010011).

Appendix A. Supporting information

Supplementary data associated with this article can be found in the online version at doi:10.1016/j.apcatb.2024.124164.

References

- [1] D. Hansora, J.W. Yoo, R. Mehrotra, W.J. Byun, D.J. Lim, Y.K. Kim, E. Noh, H. Lim, J.W. Jang, S.I. Seok, J.S. Lee, All-perovskite-based unassisted photoelectrochemical water splitting system for efficient, stable and scalable solar hydrogen production, *Nat. Energy* (2024) 1–13.
- [2] P. Zhou, I.A. Navid, Y.J. Ma, Y.X. Xiao, P. Wang, Z.W. Ye, B.W. Zhou, K. Sun, Z. T. Mi, Solar-to-hydrogen efficiency of more than 9% in photocatalytic water splitting, *Nature* 613 (2023) 66–70.
- [3] V. Andrei, G.M. Ucoski, C. Pornrungraj, C. Uswachoke, Q. Wang, D.S. Achilleos, H. Kasap, K.P. Sokol, R.A. Jagt, H.J. Lu, T. Lawson, A. Wagner, S.D. Pike, D. S. Wright, R.L.Z. Hoye, J.L.M. Driscoll, H.J. Joyce, R.H. Friend, E. Reisner, Floating perovskite-BiVO₄ devices for scalable solar fuel production, *Nature* 608 (2022) 518–522.
- [4] V. Andrei, R.A. Jagt, M. Rahaman, L. Lari, V.K. Lazarov, J.L.M. Driscoll, R.L. Z. Hoye, E. Reisner, Long-term solar water and CO₂ splitting with photoelectrochemical BiOI-BiVO₄ tandems, *Nat. Mater.* 21 (2022) 864–868.
- [5] B.W. Zhou, Y.J. Ma, P.F. Ou, Z.W. Ye, X.Y. Li, S. Vanka, T. Ma, H.D. Sun, P. Wang, P. Zhou, J.K. Cooper, Y.X. Xiao, I.A. Navid, J. Pan, J. Song, Z.T. Mi, Light-driven synthesis of C₂H₆ from CO₂ and H₂O on a bimetallic AuIr composite supported on InGaN nanowires, *Nat. Catal.* 6 (2023) 987–995.
- [6] M. Rahaman, V. Andrei, D. Wright, E. Lam, C. Pornrungraj, S. Bhattacharjee, C. M. Pichler, H.F. Greer, J.J. Baumberg, E. Reisner, Solar-driven liquid multi-carbon fuel production using a standalone perovskite-BiVO₄ artificial leaf, *Nat. Energy* 8 (2023) 629–638.
- [7] X. Guan, S. Erşan, X.C. Hu, T.L. Atallah, Y.C. Xie, S.T. Lu, B.C. Cao, J.W. Sun, K. Wu, Y. Huang, X.F. Duan, J.R. Caram, Y. Yu, J.O. Park, C. Liu, Maximizing light-driven CO₂ and N₂ fixation efficiency in quantum dot-bacteria hybrids, *Nat. Catal.* 5 (2022) 1019–1029.
- [8] J. Yuan, S. Tsujikawa, Characterization of sol-gel-derived TiO₂ coatings and their photoeffects on copper substrates, *Electrochem. Soc.* 142 (1995) 3444–3450.
- [9] B.R. Hou, X.G. Li, X.M. Ma, C.W. Du, D.W. Zhang, M. Zheng, W.C. Xu, D.Z. Lu, F. B. Ma, The cost of corrosion in China, *npj Mater. Degrad.* 1 (2017).
- [10] Z. Xing, Z.J. Wang, S.H. Yang, Capturing solar energy for cathodic protection of metals: the life of photoexcited charge carriers, *Adv. Energy Sustain. Res.* 3 (2022) 22001434.
- [11] J. Jing, Z. Chen, Y. Bu, M. Sun, W. Zheng, W. Li, Significantly enhanced photoelectrochemical cathodic protection performance of hydrogen treated Cr-doped SrTiO₃ by Cr⁶⁺ reduction and oxygen vacancy modification, *Electrochim. Acta* 304 (2019) 386–395.
- [12] M.M. Momeni, M. Motalebian, Y. Ghayeb, M. Atapour, Photoelectrochemical cathodic protection of stainless steel using W- and Cr-doped/codoped TiO₂ nanotube thin film photoanodes, *J. Electrochem. Soc.* 168 (2021) 081504.
- [13] W.F. Li, L.C. Wei, T. Shen, Y.N. Wei, K.J. Li, F.Q. Liu, W.H. Li, Ingenious preparation of “layered-closed” TiO₂-BiVO₄-CdS film and its highly stable and sensitive photoelectrochemical cathodic protection performance, *Chem. Eng. J.* 429 (2022) 132511.
- [14] Y.P. Liu, J.M. Lu, W.L. Zhang, C.Z. Lin, Z.Y. Wang, X. Wang, H. Xu, J.T. Feng, B. Hou, W. Ya, Z.J. Ren, Efficient photocathodic protection enabled by a multi-dimensional quaternary hybrid superstructure, *Chem. Eng. J.* 421 (2021) 127858.
- [15] D.W. Xu, Y. Liu, Y.H. Zhang, Z.Y. Shi, M.K. Yang, C. Zhang, B. Liu, Fabrication of pyramid-BiVO₄/CdSe composite with controlled surface oxygen vacancies boosting efficient carriers’ separation for photocathodic protection, *Chem. Eng. J.* 393 (2020) 124693.
- [16] C. Feng, Z. Chen, J. Jing, M. Sun, G. Lu, J. Tian, J. Hou, A novel TiO₂ nanotube arrays/MgTi₂O₇ multiphase-heterojunction film with high efficiency for photoelectrochemical cathodic protection, *Corros. Sci.* 166 (2020) 108441.
- [17] M. Feng, Y. Liu, S. Zhang, Y. Liu, N. Luo, D. Wang, Carbon quantum dots (CQDs) modified TiO₂ nanorods photoelectrode for enhanced photocathodic protection of Q235 carbon steel, *Corros. Sci.* 176 (2020) 108919.
- [18] Z.C. Guan, H.P. Wang, X. Wang, J. Hu, R.G. Du, Fabrication of heterostructured β-Bi₂O₃-TiO₂ nanotube array composite film for photoelectrochemical cathodic protection applications, *Corros. Sci.* 136 (2018) 60–69.
- [19] X. Jiang, M. Sun, Z. Chen, J. Jing, C. Feng, High-efficiency photoelectrochemical cathodic protection performance of the TiO₂/AgInSe₂/In₂Se₃ multijunction nanosheet array, *Corros. Sci.* 176 (2020) 108901.
- [20] C.L. Wang, W. Gao, N.Z. Liu, Y. Xin, X.Y. Liu, X.T. Wang, Y. Tian, X.W. Chen, B. R. Hou, Covalent organic framework decorated TiO₂ nanotube arrays for photoelectrochemical cathodic protection of steel, *Corros. Sci.* 176 (2020) 108920.
- [21] X. Wang, Z.C. Guan, P. Jin, Y.Y. Tang, G.L. Song, G.K. Liu, R.G. Du, Facile fabrication of BiVO₄ modified TiO₂ nanotube film photoanode and its photocathodic protection effect on stainless steel, *Corros. Sci.* 157 (2019) 247–255.
- [22] Z. Zhang, J.T. Yates, Band bending in semiconductors: chemical and physical consequences at surfaces and interfaces, *Chem. Rev.* 112 (2012) 5520–5551.

- [23] F.A.L. Laskowski, M.R. Nellist, J. Qiu, S.W. Boettcher, Metal oxide/(oxy)hydroxide overlayers as hole collectors and oxygen-evolution catalysts on water-splitting photoanodes, *J. Am. Chem. Soc.* 141 (2019) 1394–1405.
- [24] H. Xie, L. Amirav, Z. Xing, Modular design of solar-powered photocathodic metal protection device, *Carbon Neutrality* 2 (2023) 29.
- [25] G. Boschloo, Can alternative module design help to overcome stability problems of perovskite photovoltaics? *ACS Energy Lett.* 8 (2023) 1147–1151.
- [26] H. Yu, J. Wang, Q. Zhou, J. Qin, Y. Wang, X. Lu, P. Cheng, Semi-transparent organic photovoltaics, *Chem. Soc. Rev.* 52 (2023) 4132–4148.
- [27] D. Luo, R. Su, W. Zhang, Q. Gong, R. Zhu, Minimizing non-radiative recombination losses in perovskite solar cells, *Nat. Rev. Mater.* 5 (2019) 44–60.
- [28] R. Li, X. Liu, J.Z. Chen, Opportunities and challenges of hole transport materials for high-performance inverted hybrid-perovskite solar cells, *Exploration* 3 (2023) 20220027.
- [29] M. Cai, Y.X. Wei, Y.K. Li, S.B. Wang, G.S. Shao, P. Zhang, 2D semiconductor nanosheets for solar photocatalysis, *EcoEnergy* 1 (2023) 248–295.
- [30] C. Cui, X.L. Zhao, X.W. Su, N. Xi, X.N. Wang, X.W. Yu, X.L. Zhang, H. Liu, Y. H. Sang, Porphyrin-based donor-acceptor covalent organic polymer/ZnIn₂S₄ Z-scheme heterostructure for efficient photocatalytic hydrogen evolution, *Adv. Funct. Mater.* 32 (2022) 2208962.
- [31] M.Q. Yang, Y.J. Xu, W. Lu, K. Zeng, H. Zhu, Q.H. Xu, G.W. Ho, Self-surface charge exfoliation and electrostatically coordinated 2D hetero-layered hybrids, *Nat. Commun.* 8 (2017) 14224.
- [32] L.X. Meng, J.L. He, X.L. Zhou, K.M. Deng, W.W. Xu, P. Kidkhunthod, R. Long, Y. B. Tang, L. Li, Atomic layer deposition triggered Fe-In-S cluster and gradient energy band in ZnInS photoanode for improved oxygen evolution reaction, *Nat. Commun.* 12 (2021) 5247.
- [33] M. Gong, Y. Li, H. Wang, Y. Liang, J.Z. Wu, J.J. Zhou, J. Wang, T. Regier, F. Wei, H. J. Dai, An advanced Ni-Fe layered double hydroxide electrocatalyst for water oxidation, *J. Am. Chem. Soc.* 135 (2013) 8452–8455.
- [34] J.S. Luo, J.H. Im, M.T. Mayer, M. Schreier, M.K. Nazeeruddin, N.G. Park, S. D. Tilley, H.J. Fan, M. Gratzel, Water photolysis at 12.3% efficiency via perovskite photovoltaics and Earth-abundant catalysts, *Science* 345 (2014) 593–597.
- [35] Y.M. An, Z. Xing, K.C. Zhu, H. Lin, H.B. Su, S.H. Yang, Anomalous photoinduced reconstructing and dark self-healing processes on Bi₂O₂S nanoplates, *J. Phys. Chem. Lett.* 11 (2020) 7832–7838.
- [36] Y. Bu, J.P. Ao, A review on photoelectrochemical cathodic protection semiconductor thin films for metals, *Green. Energy Environ.* 2 (2017) 331–362.
- [37] M. Arnaud, Immersed cathodic protection design, in: P.M. Chess, J.P. Broomfield (Eds.), *Cathodic Protection of Steel in Concrete*, Taylor & Francis, 2010, pp. 88–89. . ISBN: 9780203938072.
- [38] C. Christodoulou, G. Glass, J. Webb, S. Austin, C. Goodier, Assessing the long term benefits of Impressed Current Cathodic Protection, *Corros. Sci.* 52 (2010) 2671–2679.
- [39] M.S. Anwa, B. Sujitha, R. Vedalakshmi, Light-weight cementitious conductive anode for impressed current cathodic protection of steel reinforced concrete application, *Constr. Build. Mater.* 71 (2014) 167–180.
- [40] Y.X. Chen, H. Xie, M. Ma, Z. Xing, Simultaneous H₂ fuel evolution and value-added organic transformation from a one-dimensional noble-metal-free photocatalyst with spatially separated catalytic sites, *Appl. Catal. B* 342 (2024) 123433.
- [41] Y.X. Chen, M. Ma, J. Hu, Z. Chen, P. Jiang, L. Amirav, S.H. Yang, Z. Xing, Coherent nanointerface between light-harvesting and catalytic transition metal sulfides for efficient photochemical conversion, *Appl. Catal., B* 324 (2023) 122300.
- [42] Z. Xing, J. Hu, M. Ma, H. Lin, Y.M. An, Z.H. Liu, Y. Zhang, J.Y. Li, S.H. Yang, From one to two: in situ construction of an ultrathin ²D–²D closely bonded heterojunction from a single-phase monolayer nanosheet, *J. Am. Chem. Soc.* 141 (2019) 19715–19727.
- [43] A. Ali, M. Kazici, S. Bozar, M.A. Asghar, N. Alwadai, C. Kahveci, M. Iqba, A. Ahma, B. Keski, M. Shahbaz, M. Kalel, S. Akyürekli, S. Günes, Super aligned carbon nanotubes for interfacial modification of hole transport layer in polymer solar cells, *Sustain. Mater. Technol.* 35 (2023) e00569.
- [44] G.D.M.R. Dabera, K.D.G.I. Jayawardena, M.R.R. Prabhath, I. Yahya, Y.Y. Tan, N. A. Nismy, H. Shiozawa, M. Sauer, G. Ruiz-Soria, P. Ayala, V. Stolojan, A.A.D. T. Adikaari, P.D. Jarowski, T. Pichler, S.R.P. Silva, Hybrid carbon nanotube networks as efficient hole extraction layers for organic photovoltaics, *ACS Nano* 7 (2013) 556.
- [45] Y. Yoon, B. Yan, Y. Surendranath, Suppressing ion transfer enables versatile measurements of electrochemical surface area for intrinsic activity comparisons, *J. Am. Chem. Soc.* 140 (2018) 2397–2400.